

COVER PAGE

Document downloaded by @DAEL

Sat Nov 28 19:05:37 2026
For personal use

When automatic English translation is provided, only the original document is authentic.
The EAA cannot be held responsible of any translation error

Bibliographical reference

Predicting Sound Absorption of Stacked Spheres: Combining an Analytical and Numerical Approach, M. Bezemer-Krijnen, Y. H. Wijnant and A. De Boer, Acta Acustica **vol. 102** (Number 6), 2016, pp. 971-983

DOI
https://doi.org/10.3813/AAA.919012

Acta Acustica united with Acustica
Vol. 102 (2016) 971 – 983

Scientific Papers
DOI 10.3813/AAA.919012

Predicting Sound Absorption of Stacked Spheres: Combining an Analytical and Numerical Approach

M. Bezemer-Krijnen, Y. H. Wijnant, A. de Boer
Faculty of Engineering Technology, University of Twente, P.O. Box 217, 7500 AE Enschede, The Netherlands.
m.bezemer@utwente.nl

Summary
Tire-road noise is a serious problem, but can be significantly reduced by the use of porous asphalt concrete. Here, the sound absorption of the porous asphalt concrete is important and can be predicted by ground impedance models. Yet, modeling porous asphalt concrete is complex, especially when nonlocal effects and scattering effects are considered. The objective of this research is to predict the sound absorption coefficient for a three-dimensional porous structure. The proposed solution is obtained using a novel modeling approach, in which the total solution of the sound field is found by combining the solutions of two subsystems: a background sound field and a scattered sound field. The background sound field contains the (analytical) solution of the sound field including the viscothermal energy dissipation inside the pores of the porous asphalt concrete. In the second subsystem, the (numerical) solution for the scattering on the rigid stone skeleton of the pavement is found. For both subsystems, we use a model containing two layers: an air layer and a viscous air layer with a certain granular structure. The main advantage of this modeling approach is the (relatively) low computation time. In this paper, the proposed modeling approach and the validation of this approach are described. The modeling approach is validated for normal incident plane waves absorbed and scattered by various structures of stacked marbles, using the impedance tube technique. This approach can be applied to predict the absorption coefficient of porous structures, like asphalt concrete roads. Moreover, it can be used as design tool to optimize the sound absorption of new road surfaces.

PACS no. 43.20.El, 43.20.Gp, 43.20.Mv, 43.40.Rj, 43.20.Tb

1. Introduction

Tire-road noise is a serious problem in (densely) populated areas. Much research has been done to predict both the sound radiation from rolling tires and the sound absorption of ground surfaces.

Sound propagation above ground surfaces and sound absorption of ground surfaces can be implemented in a BEM model, by modeling an impedance plane using the half-space notation (e.g. [1, 2]). However, this assumes a locally reacting surface while porous asphalt concrete is best described as an extended reacting surface with hard backing [3, pp. 39–50]. This can be implemented using a multi-domain BEM approach, in which the air and the porous asphalt concrete are modelled as two coupled domains (e.g. [4, 5, 6]).

For both methods – the impedance plane method and the two-domain BEM approach – the acoustic properties of the porous asphalt concrete have to be described. This is generally done using a ground impedance model, in which a distinction is made between (semi-)empirical, phenomenological models and microstructural models. In (semi-)empirical models, the model parameters are fitted to measurement results. For the majority of these models, only one or two parameters have to be known or measured. A well-known empirical ground impedance model is the Delany and Bazley model [7]. In this model, the impedance and sound absorption coefficient are described as function of the frequency and flow-resistance. This model is not directly applicable to porous asphalt concrete, since Delany and Bazley mainly tested fibrous materials with a porosity close to one. However, with some adjustments, the model gives acceptable results for outdoor surface impedances [3, pp. 62– 63].

In phenomenological models, the phenomena inside the porous material are considered on a global scale and the parameters needed for these models are often determined by measurements. It is possible to include viscothermal effects in phenomenological models. The Hamet model (e.g. [3, 8, 9]) is an extended phenomenological model, for which only three parameters are needed to describe the material. The Hamet model is often used to describe porous asphalt concrete and includes frequency dependent viscous and thermal effects.

Received 29 March 2016,
accepted 22 August 2016.

© S. Hirzel Verlag · EAA

The last type of ground impedance models are the microstructural models. This model approach is based on analytical descriptions of the (simplified) microstructure of the porous material, such as pores filled with air in an elastic or rigid frame. The pressure and velocity inside these pores are described analytically and both the thermal and the viscous dissipation of energy are included. Many microstructural models are available. More information about microstructural models is given by e.g. [3, 10].

Since there are many ground impedance models available and it is not within the scope of this paper to describe them all, the reader is referred to the overview given in [11]. In this overview, it is stated that one of the difficulties with ground impedance models are the number of parameters needed to describe the porous material accurately. When the authors [11] choose the most suitable ground impedance model, this choice was partly based on the limited number of parameters needed to describe porous asphalt surfaces.

A method to find these parameters without measurements, is to combine a ground impedance model with an additional model describing a repetitive structure that represents the porous material. This extra model can be based on analytical relations, as described by [12] for a packing of spheres, or based on a finite element model [13, 14]. The advantage of using finite element methods is that more complex geometries of the repetitive structure can be used.

1.1. Objective

The objective of this research is to develop a modeling approach which can be used to predict the acoustic behavior, such as sound absorption, for porous roads in the design phase. In this approach, the porous asphalt concrete should be modelled including local effects such as viscothermal energy dissipation inside the pores between the stones and scattering on the stones within the road surface.

The common denominator of most existing models and modeling approaches is that they consider the porous road surface as a homogeneous medium, for which the acoustic properties are valid for the entire porous road surface. In these models, the pressure and particle velocity are defined for a single pore within a rigid or flexible bulk material. The properties obtained for an individual pore are then used to find a generalized model for the entire porous material, for example by using shape factors and the porosity of the material. Therefore, the properties of the individual pore segments and pores are averaged; the porous medium is assumed to be homogeneous.

With these models, the effects of local behavior cannot be distinguished and the behavior for oblique incident waves is fixed. However, rolling tires will radiate sound in all directions and the effects of the nonlocal surface behavior should be included.

One possible modeling approach to predict the effects of nonlocal effects and behavior for oblique incidence is given by [15] for an absorber with a periodic structure, which can be a rigid frame with slits filled with absorbing material. The author of this paper describes, analytically, the scattered waves and reflected waves in terms of Hartree harmonics. While this modeling approach takes into account the nonlocal behavior of the material, it is quite complex to apply it for porous asphalt concrete, since the geometry has to be described by Hartree harmonics.

Therefore, the method we propose is to solve the scattered sound field using a finite element model. This modeling approach combines the analytical description of an undisturbed background sound field, including a viscous medium, with a finite element model to include the scattering on the stones in the porous asphalt concrete. In this approach, the properties of the viscous layer are based on the properties of the sound field inside a single pore. The approach and the resulting three-dimensional model are described in this paper. With this model, it is possible to predict the sound absorption for specified structures within the asphalt concrete and for oblique incident waves. Furthermore, it can be used as design tool to study the influence of the stone sizes in asphalt gradings, the effect of multiple layers of different gradings and the absorption for oblique incident waves.

Note that the porous asphalt concrete is assumed to be rigid and vibrations introduced by the rolling of the tyre are not included. Also, possible coupling between acoustic vibrations and structural vibrations are not taken into account.

1.2. Outline

An overview of the developed modeling approach, implementation and an example is given in Section 2. The modeling approach is validated for normal incident plane waves using an impedance tube. Therefore, in this paper, we explain the modeling approach for normal incidence, but the developed approach can also be used for oblique incident waves, as is shown by [16]. Furthermore, we focus on the sound absorption of a simplified rigid granular structure, since the model is validated for various structures of stacked marbles, as described in Section 3. The conclusions and recommendations are given in Section 4.

2. Theory

In Section 2.1, the modeling approach and the solution for the background sound field, the scattered sound field and the combined total sound field are discussed. The implementation of this approach is described in Section 2.2 and an example is given in Section 2.3.

2.1. Modeling approach

A schematic view of the proposed modeling approach with the two subsystems is given in Figure 1.

The background sound field is solved analytically using a microstructural model and the scattered sound field is solved numerically using finite element methods. The background and scattered fields are summed to find the total solution, hence including both the viscothermal effects and the scattering effects.

For both the background and scattered field, a model consisting of two layers with acoustically hard backing is implemented. The first layer consists of air and the second of viscous air. In the numerical model used for the solution of the scattered field, a schematic model of the stone structure is included in the viscous air layer. This stone structure represents the porous asphalt concrete and is modelled such that only the viscous air between the stones in this structure is considered.

Both the background and scattered sound field are solved by the Helmholtz equation [17],

$$\nabla^2\Phi + k_i^2\Phi = 0, \tag{1}$$

where ∇ is the Laplace operator, Φ is the velocity potential and k_i is the complex wave number of the ith layer. The wavenumber in the first layer, medium I, is $k_\mathrm{I} = k$; the wave number assuming standard air conditions. The wave number used in the Helmholtz equation of the second layer k_II (Equation A9) includes the viscothermal properties of this medium. These properties are based on the so-called low-reduced frequency (LRF) model (e.g. [18, 19, 20, 21]), which are described in more detail in Appendix A1. The LRF approach is similar to that of a microstructural model approach, but can be applied to a broader scope of problems. Furthermore, the applications of the LRF approach are not limited to predicting the impedance and sound absorption of porous ground surfaces. Note that any ground impedance model, as long as the viscothermal energy dissipation is included, can be used to describe the properties of the viscous air layer in this proposed hybrid modelling approach.

However, in contrast to the usual implementation, in the proposed approach the characteristic impedance and viscothermal wave propagation coefficient for a single cylindrical pore are directly used in both subsystems. For the analytical solution of the background field this is also an homogenisation of the properties, but when combined with the scattered field the nonlocal effects of the porous asphalt concrete structure are included. Therefore, this modeling approach can be used to study the influence of various parameters during the design phase of porous asphalt road surfaces. One can think of the influence of stone sizes in asphalt gradings, the effect of multiple layers of different gradings and the influence of oblique incident waves on the sound absorption.

Another advantage of this method is that the computational time is kept relatively low. The background field is solved efficiently using analytical expressions and the evaluated volume in the finite element model is small, since the scattered sound field is local.

2.1.1. Background sound field

The background sound field is based on the description of the sound field in two media: medium I is assumed to have standard air properties and medium II is defined as a viscous air layer that includes viscothermal effects, but without the structure representing the porous asphalt concrete. The second medium has an acoustically hard backing. A schematic overview of the background field is shown in Figure 2.

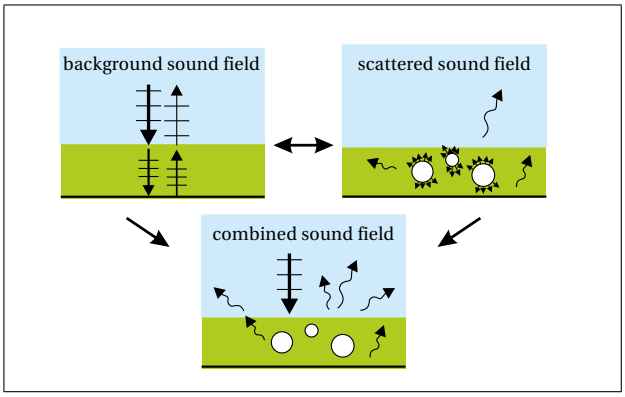

Figure 1. Schematic view of modeling approach.

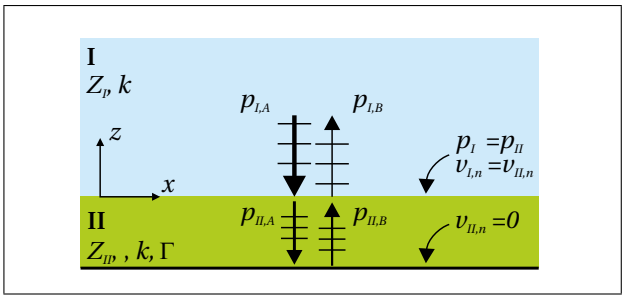

Figure 2. Schematic overview of the analytical model.

The sound field in both media is described by the sound pressure and the particle velocity, using the positive time dependence $\mathrm{e}^{\mathrm{i}\omega t}$.

The sound pressure field in the air layer (medium I) for an incoming sound wave including transmission from the viscous air layer and the reflection at the interface between the two layers is described by p_I

$$p_\mathrm{I} = A_\mathrm{I}\mathrm{e}^{\mathrm{i}kz} + B_\mathrm{I}\mathrm{e}^{-\mathrm{i}kz}, \tag{2}$$

where k is the wave number in medium I. The incident wave with complex amplitude A is travelling in the negative z-direction and the reflected waves with complex amplitude B are travelling in the positive z-direction. The particle velocity in the direction normal to the interface between medium I and medium II is given by $v_{\mathrm{I},n}$

$$v_{\mathrm{I},n} = \mathbf{v}_\mathrm{I} \cdot \mathbf{n} = \frac{-1}{Z_\mathrm{I}}\left[A_\mathrm{I}\mathrm{e}^{\mathrm{i}kz} - B_\mathrm{I}\mathrm{e}^{-\mathrm{i}kz}\right], \tag{3}$$

where Z_I is the characteristic impedance, $\mathbf{v}_\mathrm{I}$ is the particle velocity, both in medium I, and $\mathbf{n}$ is the unit vector normal to the interface between medium I and II. Medium I is assumed to have standard air properties, which yields $Z_\mathrm{I} = \rho_0 c_0$, where ρ_0 is the density of air and c_0 the speed of sound in air.

The sound pressure field in the viscous air layer (medium II) is described by p_II,

$$p_\mathrm{II} = A_\mathrm{II}\mathrm{e}^{\Gamma kz} + B_\mathrm{II}\mathrm{e}^{-\Gamma kz}, \tag{4}$$

where $\Gamma = \mathrm{i}k_{\mathrm{II}}/k$ is the viscothermal wave propagation coefficient.

The particle velocity in z-direction for the viscous air layer is given by $v_{\mathrm{II},n}$,

$$v_{\mathrm{II},n} = \mathbf{v}_{\mathrm{II}} \cdot \mathbf{n} = \frac{G}{\rho_0 c_0} \left[A_{\mathrm{II}} \mathrm{e}^{\Gamma k z} - B_{\mathrm{II}} \mathrm{e}^{-\Gamma k z} \right], \tag{5}$$

where $\mathbf{v}_{\mathrm{II}}$ is the particle velocity in medium II, and $\mathbf{n}$ is again the unit vector normal to the interface between medium I and II. The coefficient G, defined in Equation (A7), depends on the shape of the pores and includes the viscothermal effects.

Provided that the properties of the acoustic propagation (i.e. Γ and G) in the viscous air layer are known, the background sound field is completely defined once the complex amplitudes A_{I}, B_{I}, A_{II} and B_{II} are found.

The boundary conditions used to solve this problem are shown in Figure 2. The first two boundary conditions are the continuity of pressure and particle velocity in z-direction, at the interface between medium I and medium II ($z = 0$). The third boundary condition is the acoustically hard backing at the bottom of the viscous air layer, at $z = -d$, where d is the thickness of this layer. The particle velocity normal to this surface is equal to 0. To summarize,

$$p_{\mathrm{I}}|_{z=0} = p_{\mathrm{II}}|_{z=0}, \tag{6}$$

$$v_{\mathrm{I},n}|_{z=0} = v_{\mathrm{II},n}|_{z=0}, \tag{7}$$

$$v_{\mathrm{II},n}|_{z=-d} = 0. \tag{8}$$

The solution of the background sound field then yields

$$B_{\mathrm{I}} = A_{\mathrm{I}} \frac{\left(1 + \mathrm{e}^{-2\Gamma k d}\right) - G\left(1 - \mathrm{e}^{-2\Gamma k d}\right)}{\left(1 + \mathrm{e}^{-2\Gamma k d}\right) + G\left(1 - \mathrm{e}^{-2\Gamma k d}\right)}, \tag{9}$$

$$A_{\mathrm{II}} = 2A_{\mathrm{I}} \frac{1}{\left(1 + \mathrm{e}^{-2\Gamma k d}\right) + G\left(1 - \mathrm{e}^{-2\Gamma k d}\right)}, \tag{10}$$

$$B_{\mathrm{II}} = A_{\mathrm{II}} \mathrm{e}^{-2\Gamma k d}, \tag{11}$$

where the complex amplitude of the incident wave in medium I, A_{I}, is assumed known, since this amplitude is related to the wave excitation.

2.1.2. Scattered sound field

The second step in this modeling approach is solving the scattered sound field. We used a finite element method to find the sound pressure field due to the reflections on the structure of spheres. This step is indicated on the top right side of Figure 1.

The stone skeleton of the porous asphalt concrete is simplified to a structure of stacked spheres. The spheres are considered to be sound hard objects. Based on the analytical expressions of the background velocity (Equations 3 and 5) we can calculate the particle velocity due to scattering v_{scat} at the surface of the spheres,

$$v_{\mathrm{scat}} = -\mathbf{v} \cdot \mathbf{n}, \tag{12}$$

where $\mathbf{v} = \mathbf{v}_{\mathrm{I}}$ for $z \geq 0$, $\mathbf{v} = \mathbf{v}_{\mathrm{II}}$ for $z < 0$, $\mathbf{n}$ is the unit vector normal to the surface of the spheres; the tangent component is neglected. For medium II the background velocity $\mathbf{v}_{\mathrm{II}}$ – including the viscothermal effects – can be written as

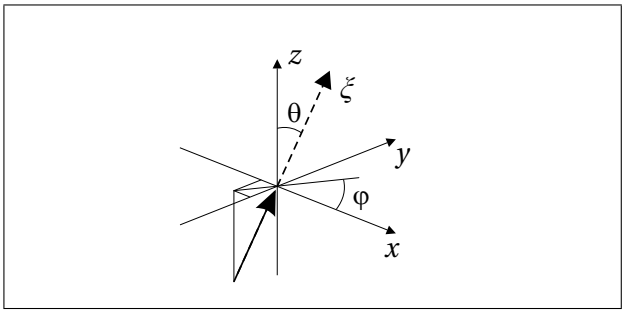

Figure 3. Conventions of direction, polar angle θ and azimuthal angle φ.

$$\mathbf{v}_{\mathrm{II}} = \frac{G}{\rho_0 c_0} \left[\mathbf{R} A_{\mathrm{II}} \mathrm{e}^{\Gamma k \xi} - \mathbf{R} B_{\mathrm{II}} \mathrm{e}^{-\Gamma k \xi} \right]. \tag{13}$$

Note that the background particle velocity is a vector, the components depend on the rotation vector,

$$\mathbf{R} = \left\{ \sin\theta \cos\varphi, \sin\theta \sin\varphi, \cos\theta \right\}'. \tag{14}$$

The spatial coordinate ξ is given by

$$\xi = x \sin\theta \cos\varphi + y \sin\theta \sin\varphi + z \cos\theta, \tag{15}$$

where x, y, z are the coordinates of a point on the outer surface of the spheres. The coordinates, the polar angle θ and azimuthal angle φ are according to the conventions shown in Figure 3.

The solution of the total sound field is found when the background field and the scattered field are summed.

2.2. Implementation

In Section 3, the model approach is validated for stacked marbles in an impedance tube. Therefore, the modeling approach is implemented for a structure of stacked spheres.

2.2.1. Schematic modeling of stone structures

The structure with the stacked spheres is a simplified representation of the stone (and bitumen) skeleton of porous asphalt concrete. At this moment, the spheres in the model all have the same dimensions and the structure of the stacked spheres is based on the hexagonal close-packed (hcp) sphere packing. In a hcp packing, the spheres are stacked in layers that have the same packing in every layer and can be written as A-B-A-B-A-B-... Each sphere is surrounded by 12 other spheres. The hcp sphere packing is shown in Figure 4.

In the future, we will implement structures which will resemble that of porous asphalt concrete more. Also, the model will be extended with additional layers, such that the sound absorption for multilayered asphalt concrete can be evaluated.

2.2.2. Properties of viscous layer

The properties of the viscous air layer (medium II), and thus the air in between the spheres, are determined using a microstructural model. We used the low reduced frequency (LRF) model, but any ground impedance model that includes the viscothermal energy dissipation will work. The LRF model is described in more detail by [18, 19, 20, 22]; some important relations are summarized in Appendix A1. The viscothermal wave propagation coefficient Γ, coefficient G, characteristic impedance Z_{II} and speed of sound c_{II} (Equations A6, A7, A11 and A12, respectively) are derived for a prismatic microstructure with circular cross-section.

The characteristic radius of this cylindrical tube is based upon the so called hydraulic tube radius r_t. We derived the hydraulic radius based on the ratio between the volume of air between the spheres and the surface area of the spheres, the 'wetted surface'. The hydraulic radius is derived for a unit cell with the hcp structure, which is defined as the smallest possible repeatable unit, containing all structural and symmetry information. For the hcp structure, the total number of spheres in the unit cell is 6. The unit cell is shown in Figure 5.

The hydraulic radius then yields

$$r_t = \frac{2V_{\mathrm{open}}}{A_{\mathrm{wetted}}} = \frac{2\left(24\sqrt{2}-8\pi\right)r^3}{24\cdot\pi r^2} = \left(\frac{2\sqrt{2}}{\pi}-\frac{2}{3}\right)r, \tag{16}$$

where V_{open} is the volume between the spheres, A_{wetted} wetted surface and r is the radius of the spheres in the unit cell.

The length of the characteristic tube and the porosity of the structure are not included as parameters in the viscous layer, since these follow directly from the FEM model of the stone structure. Therefore, the only variable needed to determine the properties of the viscous layer is the hydraulic radius of the characteristic tube.

2.2.3. Absorption coefficient

The proposed modeling approach can be used to predict the sound absorption behavior of a porous structure. The area averaged absorption coefficient α over an interface S, parallel to the interface between the medium I and medium II, is defined as the ratio of the time-averaged incident sound power W_{in} which is absorbed by this area, as described by [23]

$$\alpha = \frac{W_{\mathrm{ac}}}{W_{\mathrm{in}}} = \frac{\int \mathbf{I}_{\mathrm{ac}}\cdot\mathbf{n}\,\mathrm{d}S}{\int I_{\mathrm{in}}\,\mathrm{d}S}, \tag{17}$$

where W_{ac} is the time-averaged active sound power at S and $\mathbf{n}$ is the unit vector normal to the interface S. The active sound power is obtained by integration of the active intensity $\mathbf{I}_{\mathrm{ac}}$ over the interface S, and the incident sound power by integration of the incident intensity I_{in} over S.

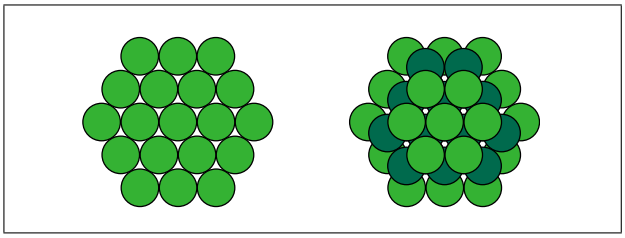

Figure 4. Stacked spheres in single layer (left) and multiple layers in hcp packing (right).

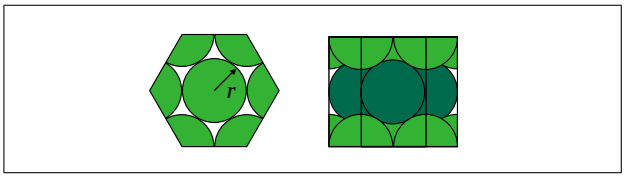

Figure 5. Schematic top view (left) and side view (right) of a unit cell for hcp packing.

The active intensity can be obtained directly from the model,

$$\mathbf{I}_{\mathrm{ac}} = \frac{1}{2}\,\mathrm{Re}\left(p\bar{\mathbf{v}}\right), \tag{18}$$

where $\bar{\mathbf{v}}$ denotes the complex conjugate of the complex particle velocity.

The complex sound pressure p is the combination of the background pressure p_{bw}, according to Equations (2) and (4) for the analytically derived background field, and the scattered pressure p_{scat}, found with the numerical model

$$p = p_{\mathrm{bw}} + p_{\mathrm{scat}}. \tag{19}$$

The incident intensity cannot be determined directly, but can be described in terms of the complex amplitude A.

$$I_{\mathrm{in}} = \frac{A\overline{A}}{2\rho_0 c_0}, \tag{20}$$

where $\overline{A}$ denotes the complex conjugate of A. The complex amplitude for the incident wave A is defined by

$$A = \frac{1}{2}\left(p - \rho_0 c_0 v_n\right), \tag{21}$$

where p is the sound pressure and v_n the particle velocity in normal direction. Note that it is assumed that the sound field can be described by local plane waves.

2.3. Example

Using the described modeling approach, a three-dimensional numerical model of an impedance tube is developed. The numerical model contains:

- Medium I (air layer): modelled as a cylinder, with perfectly matched layers (PML) at the top side.
- Medium II (viscous air layer): modelled as the air between stacked spheres.
- The walls and bottom of the cylinder representing the impedance tube are assumed acoustically hard.

Table I. Parameters of model A (with spheres of $D = 6$ mm).

Parameter	Model A
Impedance, medium I [kg/ $(m^2 s)$]	413
Speed of sound, medium I [m/s]	343
Diameter impedance tube [mm]	50
Layer height II [mm]	60
Diameter of spheres [mm]	6
Number of spheres, odd layers [-]	51
Number of spheres, even layers [-]	50
Effective tube radius r_t [mm]	0.7
Spacing δ [mm]	−0.06

The scattering problem is solved using finite elements. The model is built using the multiphysics package Comsol (version 4.4), in combination with Matlab (version 2013a). The problem is solved in the frequency domain using the MUltifrontal Massively Parallel sparse direct Solver (MUMPS); a stationary linear solver.

A model is made according to the parameters listed in Table I. The geometry of the model is shown in Figure 6. The top of the impedance tube is enclosed by perfectly matched layers (PML), such that pressure waves entering these layers are completely absorbed without reflections. PML are introduced by [24] for the application of electromagnetic waves. Other boundary conditions at the top surface of medium I are also possible, for example an impedance boundary condition, where the impedance equals $\rho_0 c_0$.

The height of medium I has to be sufficient large, such that local scattering of the sound waves, due to discretisation errors in the numerical model, are damped out at the location where the absorption coefficient is calculated.

Medium I represents the air layer and medium II represents the viscous air between the spheres. Note that this layer only contains the air between the stacked spheres, since the structure of spheres (as shown in Figure 7) is subtracted from the geometry of the impedance tube.

Since a hcp packing is used in the model, every other layer in z-direction is identical. The number of stones is given for the odd and even layers. The first layer is the top layer and the layers are numbered in negative z-direction. In Figure 7, the odd layers are shown in light green and the even layers in dark blue. The corresponding tube radius for this model is $r_t = 0.7$ mm. Using this tube radius, the viscothermal properties are derived according to Equations (A6), (A7), (A11) and (A12). Note that the LRF model returns frequency dependent properties.

2.3.1. Mesh properties

Furthermore, the mesh size of the model is studied and the meshing parameters are chosen such that for the generated mesh the solution is converged. Figure 8 shows the absorption coefficient for three variations in meshing parameters for the mesh of medium II, as listed in Table II. From this figure can be concluded that the influence of the chosen meshing parameters on the absorption coefficient is neglectably small.

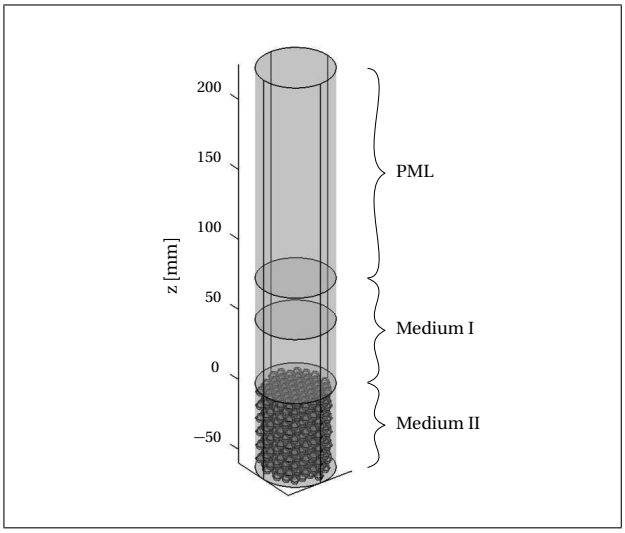

Figure 6. Geometry of numerical model with 12 layers of stacked 6 mm spheres.

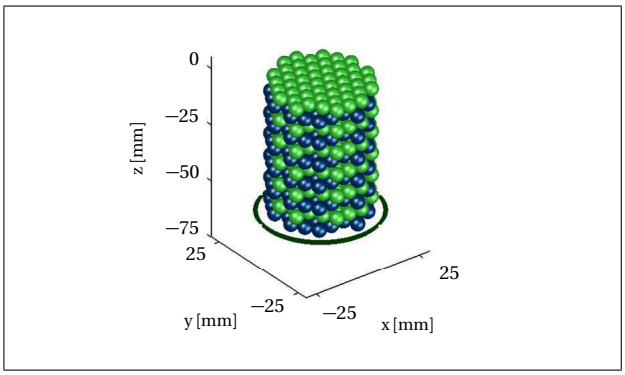

Figure 7. Stacked spheres of 6 mm diameter in hcp packing.

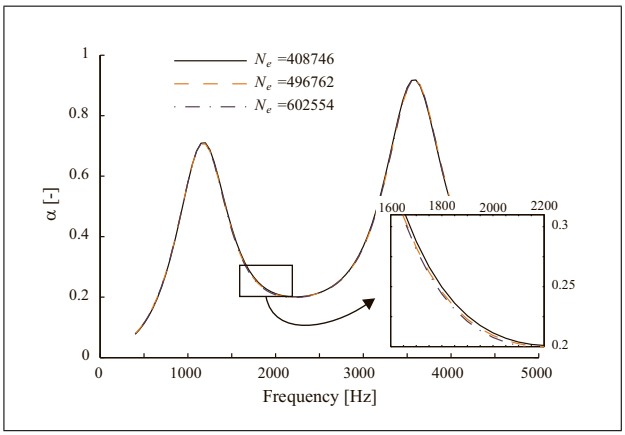

Figure 8. Absorption coefficient for three variations in meshing properties, all models contain 12 layers of stacked spheres.

It can also be concluded from Figure 8 that the mesh can be even coarser. However, meshing problems occurred while meshing the sphere structure. It is assumed that these are caused by the discretization of the spheres, as is illustrated in Figure 9. To avoid these problems, a finer mesh size is needed and a small overlap δ between the

Table II. Meshing parameters for medium II shown in Figure 8, all for model with 12 layers of stacked spheres with $D = 6$ mm.

	Model 1	Model 2	Model 3
Nr. of elem. (N_e)	408746	496762	602554
Tetrahedral elem.	408746	496762	602554
Ave. elem. quality	0.579	0.601	0.621
Min. elem. quality	1.20e-4	9.34e-5	3.14e-4
Average grow rate	2.051	1.965	1.904

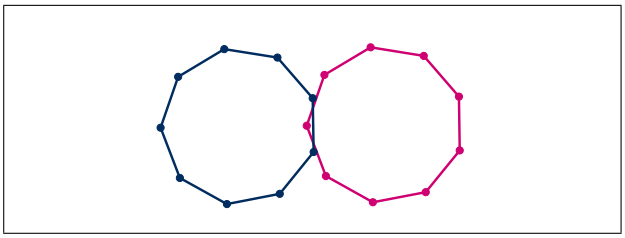

Figure 9. Discretization of the spheres.

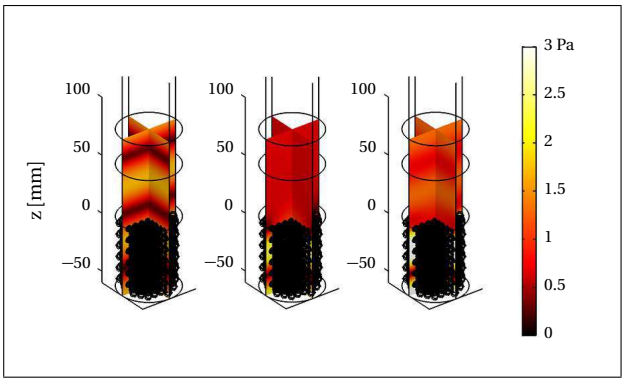

Figure 10. Solved sound pressure (amplitude) [Pa] for $D = 6$ mm, $f = 3550$ Hz: (left) incoming and reflected sound pressure; (center) scattered sound pressure and (right) total sound pressure level.

spheres is introduced, this is discussed in more detail in Section 3.1.2.

2.3.2. Results example model

Figure 10 shows the solved sound pressure fields for incident plane waves in negative z-direction, normal to the interface between medium I and II. The amplitude of the sound pressure field is shown for $f = 3550$ Hz.

On the left in Figure 10, the combined incident and reflected sound pressure field for the background field, the analytical solution, is shown. The sound pressure field of the scattered field, found with the finite element model, is shown in the center of Figure 10.

The summation of both solutions yields the total sound field, as shown on the right in Figure 10. Figure 11 shows the absolute value of the total pressure along the center of the tube in z-direction for several frequencies. The figure shows that the maximum pressure levels are found inside the viscous air layer ($z < 0$). Interesting is that for $f = 2500$ Hz, where the sound absorption coefficient is low, the

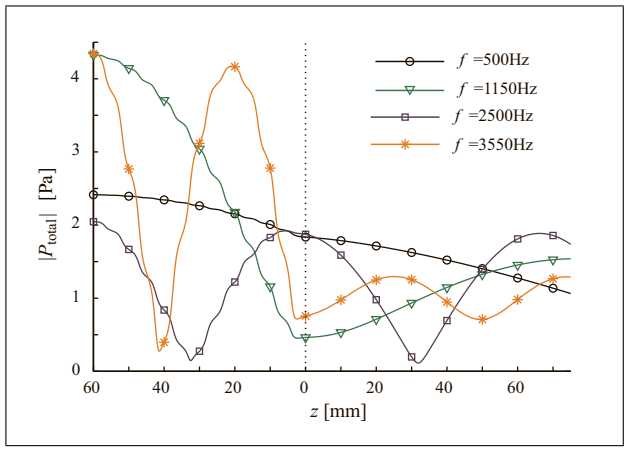

Figure 11. Total sound pressure (amplitude) for different frequencies.

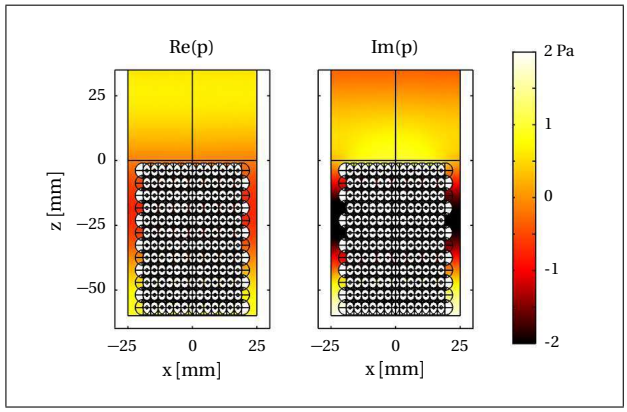

Figure 12. Detail of scattered sound pressure [Pa] for $D = 6$ mm, $f = 3550$ Hz.

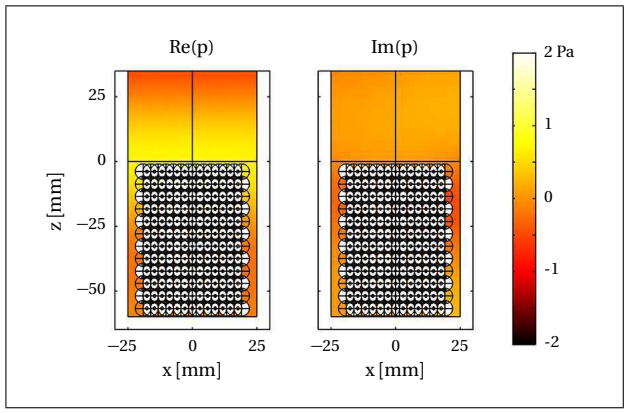

Figure 13. Detail of total sound pressure [Pa] for $D = 6$ mm, $f = 3550$ Hz.

maximum and minimum values in the viscous air layer and the air layer are of the same amplitude.

Figures 12 and 13 show the real and imaginary part of the scattered and total sound field, respectively, in more detail. It can be seen that the pressure field is changed locally around the sphere structure. Again, the maximum and minimum pressure observed in the model results are found around the sphere structure in medium II.

3. Validation with impedance tube

The modeling approach is validated with absorption measurements for various structures of stacked marbles. Figure 14 shows the impedance tube used for these measurements. The aluminium impedance tube is closed with a sound hard aluminium plate of 10 mm thickness and placed (and stabilized) in upright position.

Glass marbles were placed inside the impedance tube, the tube was slightly shaken and the stack of spheres was pressed into a more compact packing using a heavy piston. The observed stacking was slightly different than the hcp packing, due to the circular shape and small diameter of the tube. Therefore, the number of marbles and the layer height are not exactly the same as the number of spheres and layer height of the sphere structure in the models. The number of marbles is estimated based on the weight of the marbles.

The measurement results for 4 different measurements are averaged to determine the sound absorption coefficient of the stacked marbles. Two series of two measurements were performed, for both series of two measurements, the stacking of spheres is removed and rebuilt and the microphones are demounted and mounted again. Per series, the microphones are switched from position. The measurement results show very good repeatability for all 4 measurements; an average standard deviation of 0.01 was found. Figure 15 shows the measurement results for the configuration with 12 layers of stacked marbles, where the shaded area indicates ±1 of the standard deviation. This figure also shows the results of the hybrid modeling approach ('Sim.', dashed line) and the results for a microstructural model by Champoux and Stinson [9], these results are discussed in Section 3.1.1.

The impedance tube has a build-in speaker and a microphone module containing upto 4 microphones. More details about the setup and methods are given in Appendix A2.

Since the maximum frequency is kept below the cutoff frequency of the tube, only plane wave propagation is possible. Therefore, using an impedance tube, the developed model can be validated only for normal incident waves. The validation for a structure of 12 layers of glass marbles with a diameter of 6 mm is discussed in detail in Section 3.1. Here, also the sensitivity of the model results to the porosity and the tube radius used to estimate the viscothermal properties are discussed. The validation with a varying number of layers for marbles with a diameter of 6 mm and 12 mm is given in Section 3.2.

3.1. Structure with 12 layers of 6 mm marbles

The measured sound absorption coefficient for 12 layers of glass marbles of 6 mm diameter are compared to the example model from Section 2.3, which has a similar configuration.

The measurement results for this sphere packing are shown in Figure 15. The results show two distinct peaks in the absorption coefficient, similar to the type of peaks as

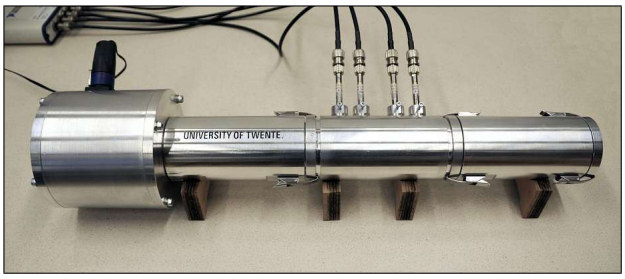

Figure 14. Impedance tube used for absorption measurements.

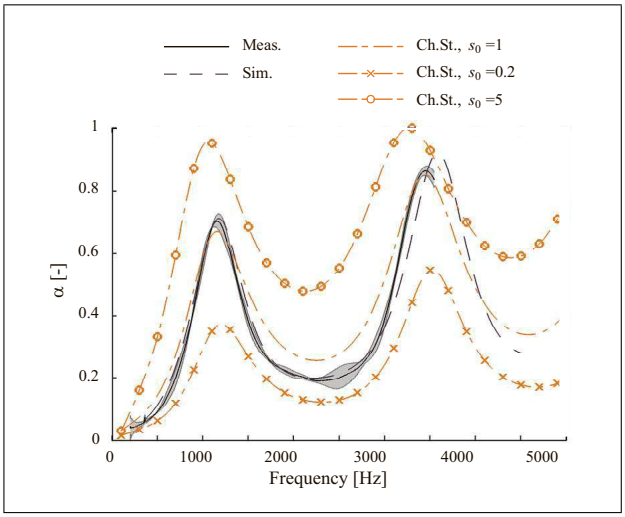

Figure 15. Measured absorption coefficient (shaded area indicates ±1 standard deviation) and predicted absorption coefficients, all for 12 layers of stacked marbles or spheres.

seen for tube resonators. The frequency of the first absorption peak is measured at $f \approx 1155$ Hz, which corresponds with a cylindrical tube resonator with a length of

$$L_{\text{eff}} = \frac{c_0}{4 f_1} \approx \frac{343}{4620} = 74\,\text{mm}, \tag{22}$$

where L_{eff} is the effective length of the resonator. As expected, this length is larger than the total height of the structure with marbles, $H \approx 61$ mm, since the pores between the marbles are curved and the traveled path of the sound waves is longer than the height of the structure.

3.1.1. Model results

The measured and predicted sound absorption coefficient are shown in Figure 15. The absorption coefficient up to about $f = 3000$ Hz is predicted extremely well by the model using the developed hybrid modelling approach. Also, the amplitude and frequency of the first peak in the absorption coefficient (at $f \approx 1155$ Hz) is similar to the measured absorption coefficient.

In Figure 15, the results are also compared to the microstructural model of Champoux and Stinson for cylindrical pores [3, 9] using the parameters in Table III. The flow resistivity R_s is derived using the Kozeny-Carman formula,

$$R_s = \frac{2\mu q^2 s_0}{(\Omega\,(r_t/2)^2)} = 1659\,\text{kg}\,\text{s}^{-1}\text{m}^{-3}, \tag{23}$$

Table III. Parameters used in Champoux and Stinson model.

Parameter		
Layer thickness	H_p	0.06m
Porosity	Ω	40%
Equivalent pore radius	r_t	0.7 mm
Tortuosity	q^2	1.9
(Steady) flow shape factor	s_0	1
Viscous shape factor	s_ρ	1
Thermal shape factor	s_k	1

where μ is the dynamic viscosity, the other parameters are accordingly to Table III, see also [3]. The first 2 parameters in this table are derived directly from the structure of the spheres. The third parameter, the equivalent pore radius (r_t), is estimated based on the geometry of the sphere structure. All three parameters are equal to the ones used in the hybrid modeling approach.

The other 4 parameters are adjustable parameters and are chosen such that the predicted absorption coefficient follows the curve of the measured absorption coefficient. These 4 adjustable parameters can be tuned based on measurements or estimated based on the geometry of the porous material. The influence of the flow resistivity on the absorption coefficient is shown by varying the (steady) flow shape factor s_0, also shown in Figure 15. Note that the flow resistivity is the only parameter which depends on this flow shape factor. For a larger flow shape factor, and thus a larger flow resistivity, the absorption coefficient increases. Also, it can be seen that the frequency of the peaks in the sound absorption coefficient shifts to a lower frequency for a larger flow resistivity.

This illustrates that the adjustable parameters introduce additional uncertainties when determining the absorption coefficient. Therefore, if a different porous material is chosen, or the structure of the porous material is varied, these parameters have to be validated again. Note that these adjustable parameters are not needed for the hybrid modeling approach, since the geometry of the porous material is used directly to find the sound field and the absorption coefficient. This makes the hybrid modeling approach more suitable as a design tool to study the influence of various (structural) properties of the porous material, like the size of the spheres or the stacking of multiple porous structures.

3.1.2. Sensitivity to porosity

As illustrated in Figure 9, it is assumed that the encountered meshing problems are caused by the discretization of the geometry of the spheres. The problems were avoided by introducing a small spacing or overlap between the spheres, δ. This spacing or overlap has as drawback that the number of spheres and thus the porosity of the sphere stacking in the model changes. This is illustrated in Figure 16 for: (left) spheres with negative spacing – an overlap of the spheres and (right) positive spacing – a gap between the spheres.

When modeling a positive spacing ($\delta > 0$) between the spheres, the total number of spheres which fit within the

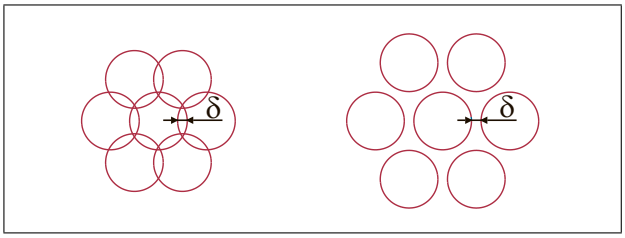

Figure 16. Overlap between spheres, $\delta < 0$ (left). Spacing between spheres, $\delta > 0$ (right).

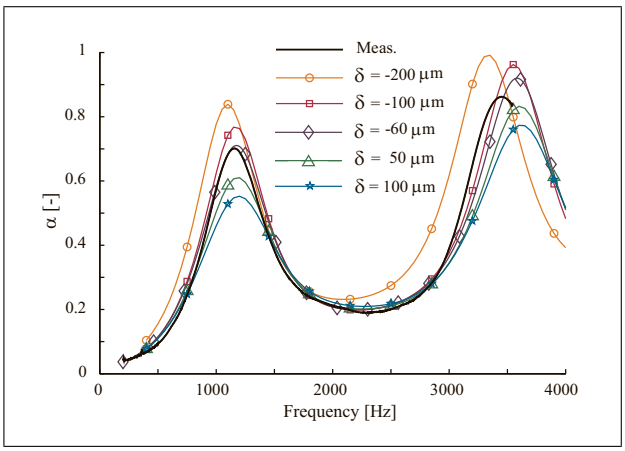

Figure 17. Sound absorption coefficient for variation in spacing between spheres.

viscous layer decreases and the porosity increases. Therefore, the maximum absorption coefficient is expected to decrease as well, since the porosity is higher than the optimal porosity. For models with a negative spacing ($\delta < 0$) it is possible to obtain the same number of spheres as marbles in the experiment. The number of spheres and marbles should agree for all models with a negative spacing. However, a difference between the number of spheres in the model and marbles in the measurements is observed. It is assumed that this is caused by differences in the sphere stacking. Note that also the layer height is slightly different.

The influence of this spacing on the sound absorption coefficient is shown in Figure 17. The parameters of the various models are listed in Table IV, where H_p is the height of the structure, N is the number of marbles or spheres and Ω is the porosity.

Figure 17 shows that the predicted sound absorption coefficients have similar curves as the measured sound absorption coefficient. The frequency of the first peak in the absorption coefficient ($f \approx 1155$ Hz) is predicted fairly well by the models. The sound absorption is best predicted by the models where the porosity and height of the structure are closest to the measurements. The best results are obtained with the model with a negative spacing of $\delta = -60\mu$m. This model predicts an absorption coefficient of $\alpha \approx 0.71$ at $f \approx 1160$ Hz, while the measured value is $\alpha \approx 0.70$ at $f \approx 1155$ Hz.

As expected, the amplitude of the absorption peak varies for the models. However, the behavior of the sound ab-

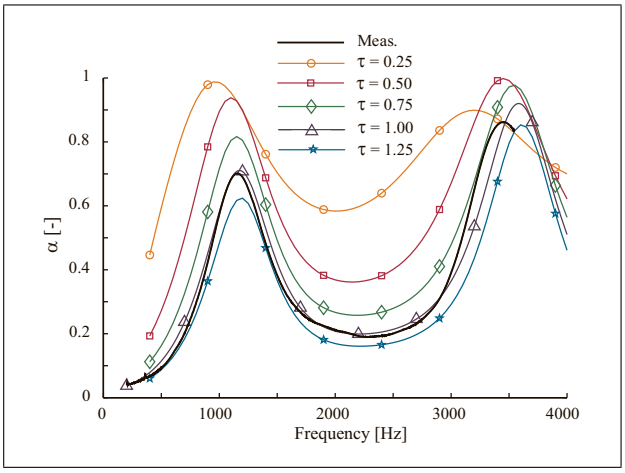

Figure 18. Sound absorption coefficient for variation in of $\tau = r_{\text{eff}}/r_t$.

sorption for the frequencies up to approximately 3000 Hz is predicted very well. The minimum value of the absorption coefficient and the slope of the curve corresponds for most models. A difference can be seen above $f = 3000$ Hz, where the frequency of the second absorption peak is predicted at a slightly higher frequency by most models. The largest differences are found for the model with $\delta = -200\mu$m; the absorption coefficient is overestimated for a large part of the frequency range. However, the frequency of the second absorption peak is predicted better.

3.1.3. Sensitivity to tube radius

The viscothermal properties of medium II are derived using the low reduced frequency model, discussed in Appendix A1. As stated in Section 2.2, the variable which determines the properties of the viscous layer is the hydraulic radius of the characteristic tube (r_t).

Since this value is an estimation of the true pore dimensions, a scaling factor is introduced,

$$r_{\text{eff}} = \tau r_t, \tag{24}$$

where τ can be seen as a shape factor to estimate the effective radius of the tube r_{eff}. The influence of this shape factor is determined with a sensitivity study.

The shape factor is varied between $\tau = 0.25$ and $\tau = 1.25$ and the predicted sound absorption is compared with the measured absorption coefficient, as shown in Figure 18. All other parameters and the structure of spheres in the three-dimensional model are kept constant. In these models a spacing of $\delta = -60\mu$m is used, which means that for $\tau = 1.00$, the model is exactly the same as the model 'Sim.: $\delta = -60\mu$m' in Section 3.1.2.

In Figure 18, it can be seen that when decreasing the value of the shape factor more sound is absorbed; this corresponds with a decreasing effective tube radius and therefore increasing viscothermal effects. For frequencies up to 3000 Hz, the model with $\tau = 1.00$, gives the best prediction of the absorption coefficient. The frequency of second peak in the sound absorption is predicted more accurately by the model with $\tau = 0.50$. However, the amplitude of this second peak is predicted better by the model with $\tau = 1.25$.

It could be possible to improve the prediction of the absorption coefficient when the spacing is chosen such that the porosity is lower and the shape factor is chosen such that the viscous effects are smaller, for example: $\delta = -100\mu$m and $\tau = 1.25$. However, finding an optimal combination of spacing and shape factor is not researched yet.

Table IV. Parameters of models for variation in spacing between spheres.

Name	H_p [mm]	N [-]	Ω [%]
Measurement	≈61	≈636	≈40
Sim.: $\delta = -200\mu$m	57	636	38
Sim.: $\delta = -100\mu$m	59	624	39
Sim.: $\delta = -60\mu$m	60	606	41
Sim.: $\delta = 50\mu$m	62	576	46
Sim.: $\delta = 100\mu$m	63	540	50

Table V. Parameters for $D = 6$ mm.

Layers	H_p [mm] Meas.	H_p [mm] Sim.	N Meas.	N Sim.
2	≈ 12	12	106	101
4	≈ 21	22	≈ 212	202
6	≈ 30	31	≈ 318	303
8	≈ 41	41	≈ 424	404
10	≈ 51	51	≈ 530	505
12	≈ 61	60	≈ 636	606
14	≈ 71	70	≈ 742	707
16	≈ 81	79	≈ 848	808

Table VI. Parameters for $D = 12$ mm.

Layers	H_p [mm] Meas.	H_p [mm] Sim.	N Meas.	N Sim.
1	≈ 612	13	12	12
2	≈ 619	23	24	24
3	≈ 631	33	36	36
4	≈ 643	42	48	48
5	≈ 654	52	60	60

3.2. Influence of marble size and number of layers

In this section, the sound absorption coefficient for various structures of stacked marbles is investigated. Two sizes of marbles are used: (a) marbles with a diameter of 6 mm and (b) marbles with a diameter of 12 mm. The parameters for the measurements and models are listed in Table V and VI for 6 mm and 12 mm marbles, respectively.

3.2.1. Validation using 6 mm marbles

Figure 19 and 20 show the absorption coefficient for structures with n layers of stacked marbles with a diameter of $D = 6$ mm. The lines with the coloured markers indicate the measured sound absorption coefficient, which is

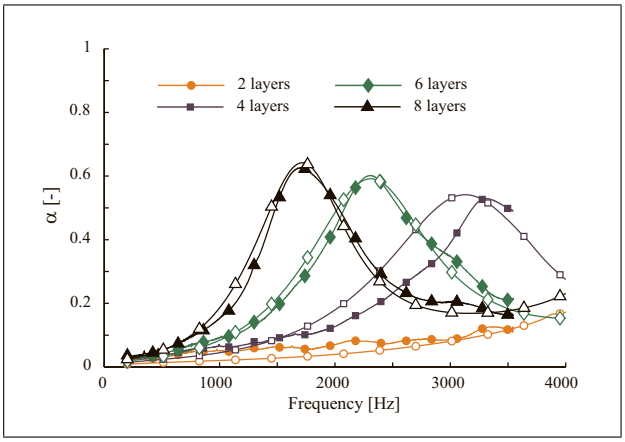

Figure 19. Measured sound absorption coefficient for stacked marbles (coloured markers online) and for predicted sound absorption coefficient (open markers) for $D = 6$ mm.

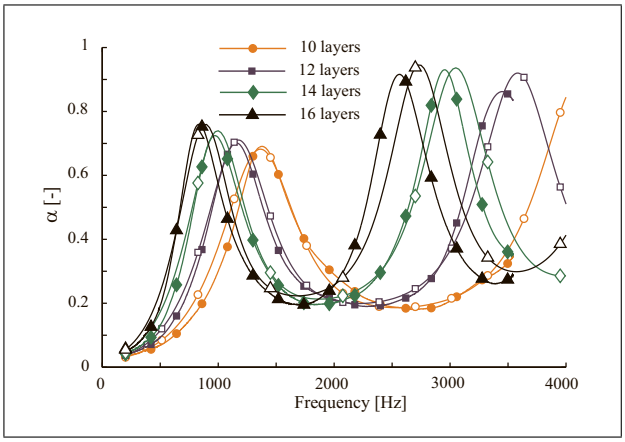

Figure 20. Measured sound absorption coefficient for stacked marbles (coloured markers online) and for predicted sound absorption coefficient (open markers) for $D = 6$ mm.

again the average of 4 measurements. The lines with the open markers indicate the predicted sound absorption coefficient for a similar structure of spheres. All models are for $\delta = -60\mu$m and $\tau = 1.00$.

The predicted sound absorption coefficient for 6 mm marbles up to the second absorption peak corresponds extremely well with the measurement results, despite the differences in the sphere packing in the model and the packing of the marbles in the measurements. Only the absorption coefficient for the model with 4 layers is predicted less well. Also, Figure 20 shows that the frequencies of the second absorption peak are predicted at a higher frequency, compared to the measurements. It is expected that the predictions of the absorption coefficient will improve when the sphere packing in the model is more similar to the packing of marbles seen in the measurements, especially when the number of marbles and layer height correspond better to the packing in the measurements.

3.2.2. Validation using 12 mm marbles

The sound absorption coefficient for marbles with a diameter of 12 mm is shown in Figure 21. Again, the lines with the coloured markers indicate the measured sound absorption coefficient and the lines with the open markers the predicted sound absorption coefficient.

The differences between the predicted and measured absorption coefficient are larger than for the 6 mm marbles, while the number of marbles and spheres in the packing does correspond exactly. The model results show that the frequency of the absorption peak is shifted to a lower frequency compared to the frequency of the measured absorption peaks. Also, the amplitude of the peaks is slightly larger for the predicted absorption coefficient. However, the predicted absorption coefficient shows the same behavior as the measured absorption coefficient.

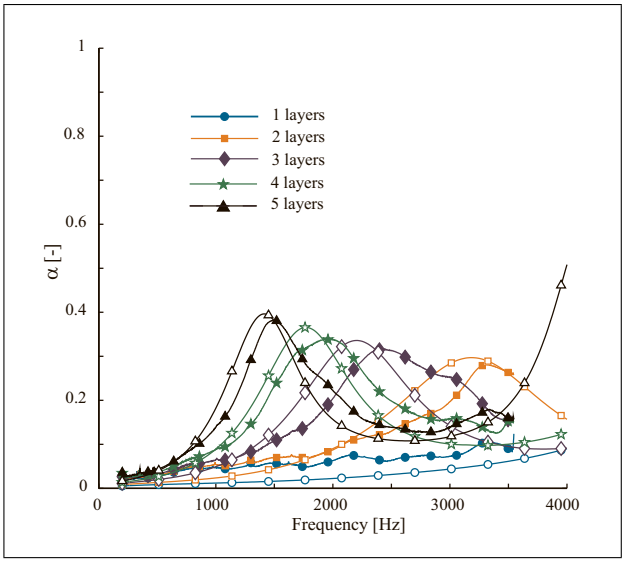

Figure 21. Measured sound absorption coefficient for stacked marbles (coloured markers online) and for predicted sound absorption coefficient (open markers) for $D = 12$ mm.

4. Conclusions and recommendations

The objective of this study was to develop a model to predict the sound absorption coefficient including both viscothermal effects and scattering effects. The modeling approach presented in this paper combines these elements. The model is validated for one-dimensional plane waves with impedance tube measurements of glass marbles and the model results closely match the measurement results.

The presented modeling approach can be used to find the absorption coefficient for existing porous asphalt roads. Furthermore, the model can be used in the process to design and manufacture new porous asphalt concretes, since the influence of individual design parameters – like stone size, stone shape, layer height and even multiple layers with different gradings – can be found directly.

In the future, the focus will be on closing the gap between the sphere structures used in the model and the stone structure in porous asphalt concrete, such that this modeling approach can be used as design tool in the development of new porous road surfaces. Also, future research will be

done on the implementation and validation for oblique incidence, using three-dimensional plane wave fields.

Appendix

A1. Low reduced frequency model

The properties of the viscous air layer are determined using the low reduced frequency (LRF) model, as described in Section 2.2.2. The LRF approach is described in detail by [18, 19, 20, 22]. The key dimensionless parameters used in the LRF model are listed below:

$$\text{shear wave number} \qquad s(\omega) = r_\mathrm{t}\sqrt{\frac{\rho_0\omega}{\mu}}, \tag{A1}$$

$$\text{ratio of specific heats} \qquad \gamma = \frac{C_p}{C_v}, \tag{A2}$$

$$\text{Prandtl number} \qquad N_\mathrm{pr} = \frac{\nu}{\alpha_t} = \frac{\mu C_p}{\kappa}. \tag{A3}$$

The shear wave number s represents the ratio between the inertial and viscous forces, where μ is the dynamic viscosity and r_t is the characteristic radius of the tube. The ratio of specific heats is the ratio between the specific heat at constant pressure C_p and at constant volume C_v. The Prandtl number is defined as the ratio between the viscous diffusion rate (denoted by the kinematic viscosity $\nu = \mu/\rho_0$) and the thermal diffusion rate (denoted by the thermal diffusivity $\alpha_t = \kappa/\left(\rho_0 C_p\right)$, where κ is the thermal conductivity).

The sound pressure $p(\omega, z)$ is given by

$$p(\omega, z) = A\mathrm{e}^{\Gamma(\omega)kz} + B\mathrm{e}^{-\Gamma(\omega)kz}. \tag{A4}$$

The solution for the velocity in axial direction, averaged over the cross-section of the tube, yields

$$\bar{v}(\omega, z) = \frac{G(\omega)}{\rho_0 c_0}\left[A\mathrm{e}^{\Gamma(\omega)kz} - B\mathrm{e}^{-\Gamma(\omega)kz}\right], \tag{A5}$$

where A and B are the complex amplitudes of the incident and reflected waves, ρ_0, c_0 and k are for standard air conditions and the coefficients Γ and G depend on the angular frequency ω as well as the geometry of the cross-section. Here, only the solution for a cylindrical cross-section is given,

$$\Gamma(\omega) = \sqrt{\frac{J_0\left(\mathrm{i}\sqrt{i}s(\omega)\right)}{J_2\left(\mathrm{i}\sqrt{i}s(\omega)\right)}\frac{\gamma}{n}}, \tag{A6}$$

$$G(\omega) = -\frac{\mathrm{i}}{\Gamma(\omega)}\frac{\gamma}{n}, \tag{A7}$$

where J_0 and J_2 are Bessels functions of the first kind of order 0 and 2. The coefficient n is given by

$$n(\omega) = \left[1 + \frac{\gamma - 1}{\gamma}\frac{J_2\left(\mathrm{i}\sqrt{iN_\mathrm{pr}}s(\omega)\right)}{J_0\left(\mathrm{i}\sqrt{iN_\mathrm{pr}}s(\omega)\right)}\right]^{-1}. \tag{A8}$$

Using the low reduced frequency description for medium II, the wave number of this medium can be derived from the viscothermal wave propagation coefficient Γ,

$$k_\mathrm{II}(\omega) = -\mathrm{i}k\Gamma(\omega). \tag{A9}$$

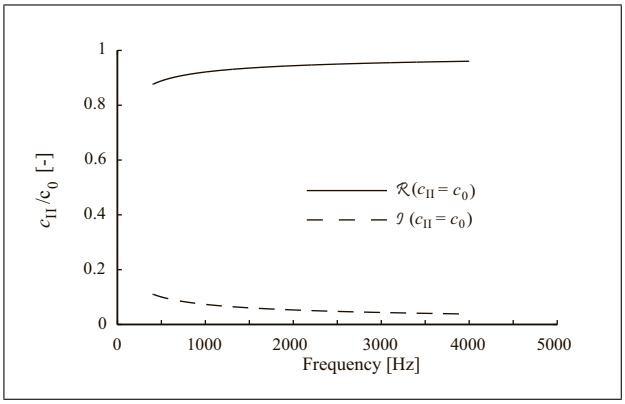

Figure A1. Ratio between speed of sound for the example model: $c_\mathrm{II}(\omega)/c_0$, real (—) and imaginary (- - -) part.

Table A1. Dimensions of impedance tube.

Parameter		Value
Inner radius tube [mm]	R	25
Outer radius tube [mm]	R_o	35
Microphone distance 1-1 [mm]	z_1	0
Microphone distance 1-2 [mm]	z_2	24
Microphone distance 1-3 [mm]	z_3	62
Microphone distance 1-4 [mm]	z_4	86
Cutoff frequency [Hz]	f_co	$c_0/(4R)$

The particle velocity in medium II can also be expressed similar to Equation (3):

$$v_{\mathrm{II},n}(\omega, z) = \frac{-1}{Z_\mathrm{II}(\omega)}\left[A_\mathrm{II}\mathrm{e}^{\Gamma(\omega)kz} - B_\mathrm{II}\mathrm{e}^{-\Gamma(\omega)kz}\right], \tag{A10}$$

where Z_II is the characteristic impedance of medium II,

$$Z_\mathrm{II}(\omega) = -\frac{\rho_0 c_0}{G(\omega)}. \tag{A11}$$

The (frequency dependent) speed of sound in medium II is determined by

$$c_\mathrm{II}(\omega) = \omega/k_\mathrm{II}(\omega). \tag{A12}$$

For the model described in Section 2.3, the ratio between the speed of sound in medium I and II, $c_\mathrm{II}(\omega)/c_0$, as function of the frequency, is shown in Figure A1.

A2. Impedance tube measurements

The impedance tube setup is shown in Figure 14. The important dimensions are summarized in Table A1.

The measured microphone signals are controlled and processed using LabView and the post processing is performed in Matlab. The signals are analysed in the frequency domain using a method based on the method described by [25]. In this paper we focus on obtaining the absorption coefficient for normal incidence, using the sound pressure from all 4 microphones.

The sound pressure for a local plane wave is given by Equation (2), where the microphone location can be denoted by z_i . The microphone locations are known (listed

in Table A1) and plane waves normal to the measurement plane are assumed. Therefore, the measured sound pressure for each microphone can be described by Equation (2) and written in matrix form,

$$\begin{Bmatrix} P_1(z_1,\omega) \\ P_2(z_2,\omega) \\ \vdots \\ P_n(z_n,\omega) \end{Bmatrix} = \begin{bmatrix} e^{ikz_1} & e^{-ikz_1} \\ e^{ikz_2} & e^{-ikz_2} \\ \vdots & \vdots \\ e^{ikz_n} & e^{-ikz_n} \end{bmatrix} \begin{Bmatrix} A(\omega) \\ B(\omega) \end{Bmatrix}, \quad \text{(A13)}$$

where ω is the angular frequency. This system can be written as

$$\mathbf{P} = \mathbf{Sa}. \quad \text{(A14)}$$

The vector $\mathbf{P}$ contains the sound pressure measured by the microphones and the vector $\mathbf{a}$ contains the unknown complex amplitudes, $A(\omega)$ and $B(\omega)$. The matrix $[\mathbf{S}]$ describes the sound field in the impedance tube at the locations of the microphones. The system is solved for the complex amplitudes, in a least square sense using the normal equations

$$\mathbf{a} = \left(\mathbf{S}^{\mathrm{T}}\mathbf{S}\right)^{-1}\mathbf{S}^{\mathrm{T}}\mathbf{P}, \quad \text{(A15)}$$

where $\mathbf{S}^{\mathrm{T}}$ is the conjugate transpose of $\mathbf{S}$.

The measured sound absorption coefficient α is then given by

$$\alpha(\omega) = 1 - |R(\omega)|^2 = 1 - \frac{B(\omega)\,\overline{B(\omega)}}{A(\omega)\,\overline{A(\omega)}}, \quad \text{(A16)}$$

where $\overline{A(\omega)}$ and $\overline{B(\omega)}$ are the complex conjugates of the complex amplitudes, $A(\omega)$ and $B(\omega)$ respectively.

Acknowledgement

This project is carried out in the framework of the innovation program 'GO Gebundelde Innovatiekracht', funded by the 'European Regional Development Fund', 'Regio Twente' and 'Provincie Overijssel'. The project partners are Apollo Tyres Global R&D, University of Twente (Tire-Road Consortium), Reef Infra, STEMMER IMAGING and the Provincie Gelderland, and their support is gratefully acknowledged.

References

[1] M. Ochmann, H. Brick: Acoustical radiation and scattering above an impedance plane. – In: Computational Acoustics of Noise Propagation in Fluids-Finite and Boundary Element Methods. Springer, 2008, 459–494.

[2] J. Schutte: Numerical simulation of tyre/road noise. Dissertation. University of Twente, 2011.

[3] K. Attenborough, K. M. Li, K. Horoshenkov: Predicting outdoor sound. Taylor & Francis, 2007.

[4] F. Anfosso-Lédée, P. Dangla: Sound propagation above a porous road surface by boundary element method. Road Materials and Pavement Design **7** (2006) 289–312.

[5] F. Anfosso-Lédée, P. Dangla, M. Bérengier: Sound propagation above a porous road surface with extended reaction by boundary element method. J. Acoust. Soc. Am. **122** (2007) 731–736.

[6] E. Sarradj: Multi-domain boundary element method for sound fields in and around porous absorbers. Acta Acustica united with Acustica **89** (2003) 21–27.

[7] M. E. Delany, E. N. Bazley: Acoustical properties of fibrous absorbent materials. Appl. Acoust. **3** (1970) 105–116.

[8] J. F. Hamet, M. Berengier: Acoustical characteristics of porous pavements: a new phenomenological model. INTER-NOISE 93: people versus noise, Leuven, Belgium, 1993, 641–646.

[9] M. C. Berengier, M. R. Stinson, G. Daigle, J. Hamet: Porous road pavements: Acoustical characterization and propagation effects. J. Acoust. Soc. Am. **101** (1997) 155–162.

[10] J. Allard, N. Atalla: Propagation of sound in porous media: Modelling sound absorbing materials 2e. John Wiley & Sons, 2009.

[11] K. Attenborough, I. Bashir, S. Taherzadeh: Outdoor ground impedance models. J. Acoust. Soc. Am. **129** (2011) 2806–2819.

[12] O. Umnova, K. Attenborough, K. M. Li: A cell model for the acoustical properties of packings of spheres. Acta Acustica united with Acustica **87** (2001) 226–235.

[13] C.-Y. Lee, M. J. Leamy, J. H. Nadler: Acoustic absorption calculation in irreducible porous media: A unified computational approach. J. Acoust. Soc. Am. **126** (2009) 1862–1870.

[14] T. G. Zielinski: Microstructure-based calculations and experimental results for sound absorbing porous layers of randomly packed rigid spherical beads (034905). J. Appl. Phys. **116** (2014).

[15] F. P. Mechel: Sound fields at periodic absorbers. J. Sound Vib. **136** (1990) 379–412.

[16] M. Bezemer-Krijnen, Y. H. Wijnant, A. de Boer: Three-dimensional modelling of sound absorption in porous asphalt pavement for oblique incident waves. Euronoise 2015, 2015.

[17] D. T. Blackstock: Fundamentals of physical acoustics. John Wiley & Sons, 2000.

[18] H. Tijdeman: On the propagation of sound waves in cylindrical tubes. J. Sound Vib. **39** (1975) 1–33.

[19] W. M. Beltman: Viscothermal wave propagation including acousto-elastic interaction. Dissertation. University of Twente, 1998.

[20] F. J. M. v. d. Eerden: Noise reduction with coupled prismatic tubes. Dissertation. University of Twente, 2000.

[21] M. H. C. Hannink., Y. H. Wijnant, A. de Boer: Optimised sound absorbing trim panels for the reduction of aircraft cabin noise. Eleventh International Congress on Sound and Vibration, ICVS 11, 2004.

[22] M. H. C. Hannink: Acoustic resonators for the reduction of sound radiation and transmission. Dissertation. University of Twente, 2007.

[23] Y. Wijnant, E. R. Kuipers, A. de Boer: Development and application of a new method for the insitu measurement of sound absorption. Proceeding of ISMA2010 including USD2010, 2010.

[24] J.-P. Berenger: A perfectly matched layer for the absorption of electromagnetic waves. J. Comput. Phys. **114** (1994) 185–200.

[25] E. R. Kuipers, Y. H. Wijnant, A. de Boer: Measuring oblique incidence sound absorption using a local plane wave assumption. Acta Acustica united with Acustica **100** (2014) 205–214.